Neoplasia • Vol. 8, No. 3, March 2006, pp. 214–222 214

www.neoplasia.com

Nanoparticle Imaging of Integrins on Tumor Cells[1]

Xavier Montet, Karin Montet-Abou, Fred Reynolds, Ralph Weissleder and Lee Josephson

Center for Molecular Imaging Research, Massachusetts General Hospital and Harvard Medical School, Charlestown, MA, USA

Abstract

Nanoparticles 10 to 100 nm in size can deliver large payloads to molecular targets, but undergo slow diffusion and/or slow transport through delivery barriers. To examine the feasibility of nanoparticles targeting a marker expressed in tumor cells, we used the binding of cyclic arginine–glycine–aspartic acid (RGD) nanoparticle targeting integrins on BT-20 tumor as a model system. The goals of this study were: 1) to use nanoparticles to image $\alpha_V\beta_3$ integrins expressed in BT-20 tumor cells by fluorescence-based imaging and magnetic resonance imaging, and, 2) to identify factors associated with the ability of nanoparticles to target tumor cell integrins. Three factors were identified: 1) tumor cell integrin expression (the $\alpha_V\beta_3$ integrin was expressed in BT-20 cells, but not in 9L cells); 2) nanoparticle pharmacokinetics (the cyclic RGD peptide cross-linked iron oxide had a blood half-life of 180 minutes and was able to escape from the vasculature over its long circulation time); and 3) tumor vascularization (the tumor had a dense capillary bed, with distances of <100 μm between capillaries). These results suggest that nanoparticles could be targeted to the cell surface markers expressed in tumor cells, at least in the case wherein the nanoparticles and the tumor model have characteristics similar to those of the BT-20 tumor employed here.

Neoplasia (2006) **8,** 214–222

Keywords: Nanoparticle, imaging, RGD, peptide, integrin.

Introduction

The quest for more potent and selective tumor-targeted diagnostic and therapeutic agents, and the widespread interest in nanotechnology have led to recent proposals that targeted nanoparticle-based pharmaceuticals might be designed to fit this need (http://nano.cancer.gov/) [1–3]. Nanoparticles offer two key advantages as targeted agents: inherent nanoparticle amplification and surface-mediated multivalent affinity effects. Inherent nanoparticle amplification refers to nanoparticle geometry consisting of a core, typically with thousands of drug molecules or detectable atoms (gold and iron), and a coating, typically consisting of a much smaller number (1–50) of targeting peptides or antibodies. For example, with magneto-fluorescent nanoparticles, there are 8000 Fe/nanoparticle [4] and 3 to 50 targeting proteins or peptides attached per nanoparticle [5,6]. A second advantage of nanoparticles is their multivalent affinity enhancement. Although multivalency can result from a variety of different mechanisms (e.g., see Figure 2 of Kitov and Bundle [7]) [8–10], nanoparticles produce multivalent effects due to multiple, simultaneous interactions between the surface of the nanoparticle and the surface of the cell. The nanoparticle used in the current study exhibits strong multivalent effects in endothelial cell adhesion assays and antiproliferative assays (Montet and Josephson, submitted for publication).

In spite of these intriguing advantages, the development of targeted nanoparticles for a large class of targets (markers expressed in tumor cells) is limited by nanoparticle size, which may limit delivery to tumor cells lying beyond the endothelial barrier of the vascular compartment. The ability to target high-molecular-weight compounds, such as monoclonal antibodies or nanoparticles, to tumor cell targets is hindered by their slow diffusion (in solution or through tissues) and/or slow transport through delivery barriers such as endothelial cells [11,12]. Nanoparticles are typically defined as materials between 10 and 100 nm, are modestly larger than antibodies, and are far larger than low-molecular-weight pharmaceuticals (<10 kDa). (IgG antibodies have a diameter of 10 nm; see Table 1 of Reynolds et al. [4]). Nanoparticles have been used to image integrins in endothelial cells, particularly the endothelial cells of angiogenic blood vessels [13–19], or to image nonintegrin targets where escape from the vasculature is not required [18,20,21].

The goals of this study were: 1) to establish that nanoparticles could be used to image a molecular marker expressed in tumor cells using an arginine–glycine–aspartic acid (RGD) magneto-optical nanoparticle as a model system and integrin-expressing tumor cells, and 2) to describe the factors that might allow materials as large as nanoparticles to reach tumor

Abbreviations: CLIO, cross-linked iron oxide; FMT, fluorescence molecular tomography; FRI, fluorescence reflectance imaging; DTT, dithiothreitol; cRGD, cyclic RGD peptide; scrRGD, scrambled RGD peptide; IRGD, linear RGD peptide

Address all correspondence to: Lee Josephson, PhD, Center for Molecular Imaging Research, Massachusetts General Hospital, Building 149, 13th Street, No. 5406, Charlestown, MA 02129. E-mail: ljosephson@partners.org

[1]This study was supported by National Institutes of Health grants P50 CA86355, R24 CA92782, and R01 EB00662. X.M. was supported by a fellowship from the Swiss National Science Foundation, and K.M.A. was supported by the Swiss National Science Foundation (grant PPOB- 68778).

Received 18 November 2005; Revised 5 January 2006; Accepted 6 January 2006.

DOI 10.1593/neo.05769

cell markers. Our results indicate that magneto-fluorescent RGD nanoparticles were targeted to $\alpha_V\beta_3$-expressing tumor cells *in vivo* and were detectable by fluorescence reflectance imaging (FRI), fluorescence molecular tomography (FMT), and magnetic resonance imaging (MRI). Factors permitting the imaging of tumor integrins included the vascularized nature of the BT-20 tumor, the long nanoparticle blood half-life, and the ability of nanoparticles to slowly escape the vasculature.

Materials and Methods

Peptide synthesis was performed with Fmoc chemistry to obtain a linear RGD peptide (lRGD) GSSK(Fl)GGGCRGDC and a scrambled RGD peptide (scrRGD) GSSK(Fl)-GGGCDRGC as C-terminal amides. A disulfide-linked cyclic RGD peptide (cRGD) was obtained by oxidation (bubbling air) of lRGD peptide at room temperature at 0.2 to 0.4 mg/ml peptide in 0.1 M ammonium bicarbonate for 24 hours.

To synthesize peptide–nanoparticle conjugates, amino cross-linked iron oxide (CLIO) nanoparticle, synthesized as described [22,23], was first reacted with the *N*-hydroxysuccinimide ester of Cy5.5 or Cy3.5 (Amersham Biosciences Corp., Piscataway, NJ) [24]. There were approximately 250 amines per amino-CLIO nanoparticle, at 8000 Fe/nanoparticle [4], with 8 to 10 amines consumed by the attachment of Cy5.5 (Figure 1*C*). This leaves the remaining amines for peptide attachment using disuccinimidyl suberimidate [25]. With the nomenclature of cRGD-CLIO(Cy5.5) for the nanoparticle, the attached peptide is given first (cyclic RGD, cRGD), followed by the CLIO abbreviation to indicate the origin of the nanoparticle, followed by the fluorochrome (Cy5.5) attached directly to the CLIO and given in parentheses. Fluorescein, attached to peptides before conjugation to the nanoparticle, does not appear in this notation; it allows characterization of the peptide/iron ratio based on its absorption at 493 nm and permits the determination of cell-associated peptide or peptide–nanoparticle as immunoreactive fluorescein [26]. When cRGD-CLIO(Cy5.5) is treated with dithiothreitol (DTT), the disulfide bond is broken and the resulting nanoparticle is denoted as lRGD-CLIO(Cy5.5) (see Figure 1*B*).

BT-20 (a human breast carcinoma cell line) and 9L (a rat gliosarcoma cell line) were obtained from the American Tissue Culture Collection (Manassas, VA) and were cultured according to the manufacturer's instructions.

To characterize the presence of $\alpha_V\beta_3$ on BT-20 cells (Figure 2), cells were trypsinized and incubated in culture media (at 37°C for 30 minutes) with Cy5.5-labeled anti-$\alpha_V\beta_3$ antibody (Abcam, Inc., Cambridge, MA) and cRGD at a final concentration of 1 μg/ml. The samples were analyzed for fluorescein and Cy5.5 fluorescence with a FACScalibur

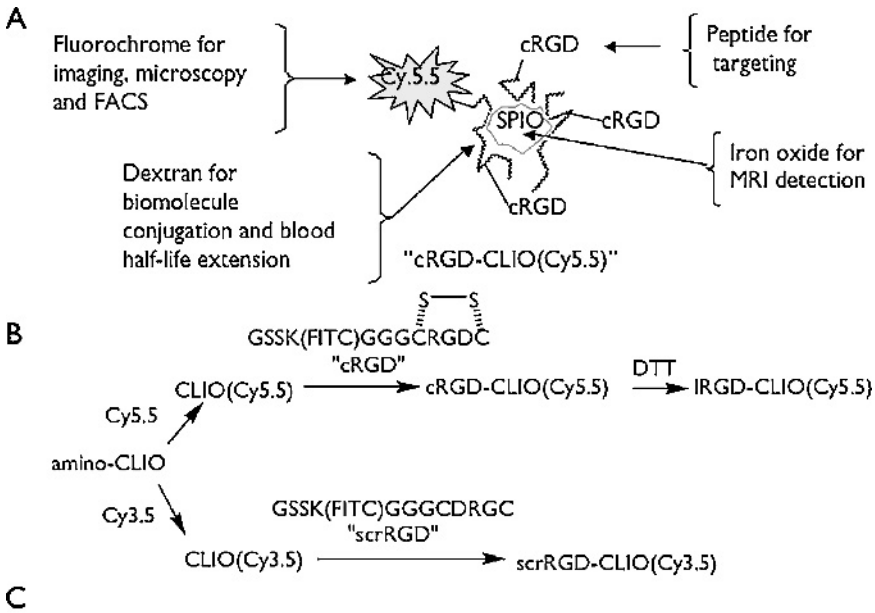

C

Properties of Nanoparticles					
Nanoparticle	Size, (nm)	Relaxivity, R2, $(mMsec)^{-1}$	Peptide/ Nano-particle	Cy5.5/ Nano-particle	Blood Half-life (min)
cRGD-CLIO(Cy5.5)	28 ± 3	111 ± 1	27.2	7.2	180±36
ScrRGD-CLIO(Cy3.5)	36 ± 8	118 ± 5	28.4	8.4	207±26

Figure 1. *Design, synthesis, and properties of nanoparticles. (A) schematic diagram of nanoparticle components and functions. (B) Synthesis of nanoparticles. DTT linearizes the disulfide-linked cRGD, linearizing the peptide to lRGD. (C) Physical properties of the nanoparticles used in this study.*

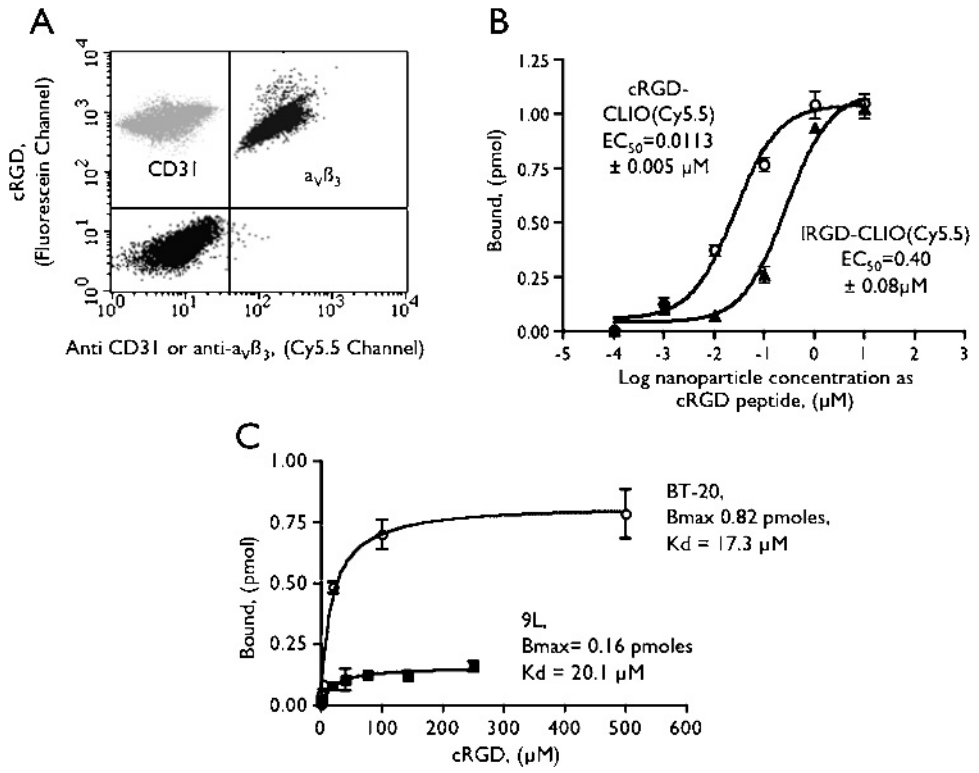

Figure 2. *Expression of $\alpha_V\beta_3$ on tumor cells. (A) Dual-wavelength FACS analysis of the binding of cRGD and anti-$\alpha_V\beta_3$ to BT-20 tumor. BT-20 cells bind anti-$\alpha_V\beta_3$ and cRGD, but not the control. (B) Uptake of the cRGD-CLIO nanoparticle by BT-20 cells. DTT treatment linearized the peptide and reduced affinity. (C) Binding of the cRGD to BT-20 and 9L cells determined as cell-associated fluorescein from fluorescein immunoassay. Values of apparent affinity constant (K_d) and binding per 1,000,000 cells are shown.*

cytometer (Becton Dickinson, Franklin Lakes, NJ). A Cy5.5-labeled anti-CD31 antibody (Santa Cruz Biotechnology, Santa Cruz, CA) was used as a control for nonspecific binding.

To determine cell-associated RGD peptide or peptide–nanoparticle (Figure 2), BT-20 cells were incubated with various peptide or peptide–nanoparticle concentrations in the media mentioned above (30 minutes, 37°C, and 5% CO_2) in six-well plates at about 1 million cells/well. Cells were then washed thrice with Hanks balanced salt solution (Mediatech, Inc., Herndon, VA) and lysed with phosphate-buffered saline containing 0.1% Triton X-100 and 1 mM 8-anilino-1-naphthalenesulfonic acid. Fluorescein isothiocythiocyanateanate concentration was determined [26]. Each experiment was performed thrice, with data points determined in triplicate.

To obtain tumors, 1 million BT-20 or 9L cells were implanted in the rear flank or mammary fat pads of nude mice (~25 g) and were imaged when tumors had reached a diameter of 3 to 4 mm (6–9 days postimplantation). Animals were then anesthesized (gas anesthesia, 2% isoflurane), and a mixture of cRGD-CLIO(Cy5.5) and scrRGD-CLIO(Cy3.5) nanoparticles was injected through the tail vein. For tissue fluorescence studies (Figure 3), the iron dose from both nanoparticles was 5 mg/kg, with the amount of each nanoparticle adjusted so that the same fluorescence from each probe was used. Animals were sacrificed 24 hours post-injection. Slices of tissues (about 1.5 mm) were place on a dark plate, and Cy5.5 and Cy3.5 tissue fluorescence was obtained with a custom-built mouse optical imaging system [27, 28], which is capable of multichannel fluorescent imaging without significant spectral overlap. Fluorescence was determined using operator-defined regions-of-interest (ROI) measurements on tissues from injected (fluorescence) and uninjected animals (autofluorescence). With autofluorescence subtracted, the Cy5.5/Cy3.5 fluorescence ratio was determined. The significance of *P* values was evaluated with ANOVA and Bonferroni test. Animals were sacrificed with injection of pentobarbital sodium (100 mg/kg, ip). All experiments were performed in accordance with the MGH Animal Care Committee.

To determine tumor/background ratios (Figure 4), three ROI were drawn. ROI were placed on the tumor (the white light image was used to place the ROI) and on the normal skin to measure signal intensity (SI). A third ROI was placed outside the animal to determine system noise. Tumor/background ratio was determined as:

$$\frac{\text{Tumor}}{\text{background}} = \frac{(\text{SI}_{\text{tumor}} - \text{Noise})}{(\text{SI}_{\text{skin}} - \text{Noise})}.$$

For FMT, we used a modular home-built scanner, the components of which have been described [29]. Image data sets were reconstructed using a normalized Born forward model [30]. Details of the algorithm have been published [31]. Excitation laser diode sources included a 672-nm laser and a 748-nm laser (BW Tek, Newark, DE). The excitation

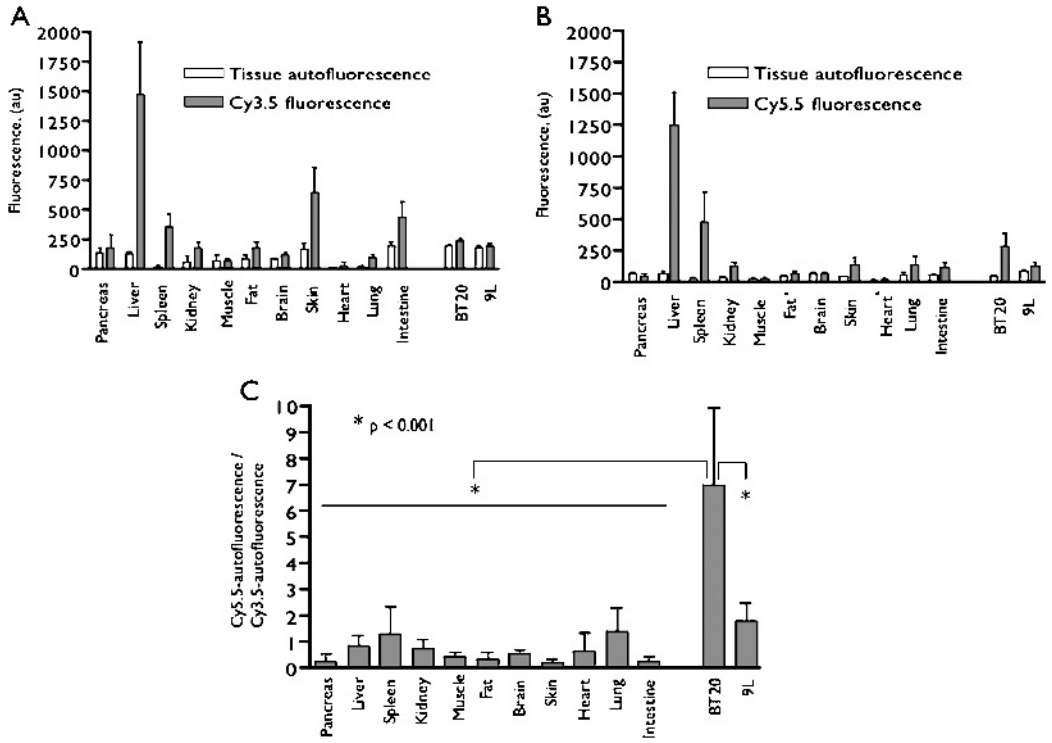

Figure 3. *Molecular specificity of the cRGD-CLIO(Cy5.5) nanoparticle* in vivo *by dual-channel tissue FRI. A mixture of cRGD-CLIO(Cy5.5) and scrRGD-CLIO(Cy3.5) was injected. (A) Cy3.5 channel fluorescence of dissected tissues. (B) Cy5.5 channel tissue fluorescence. (C) Ratio of tissue fluorescence in the Cy5.5 and Cy3.5 channels. Only the BT-20 tumor has a high ratio of Cy5.5/Cy3.5 fluorescence. The BT-20 tumor was different from all other tissues and from the 9L tumor at P < .001.*

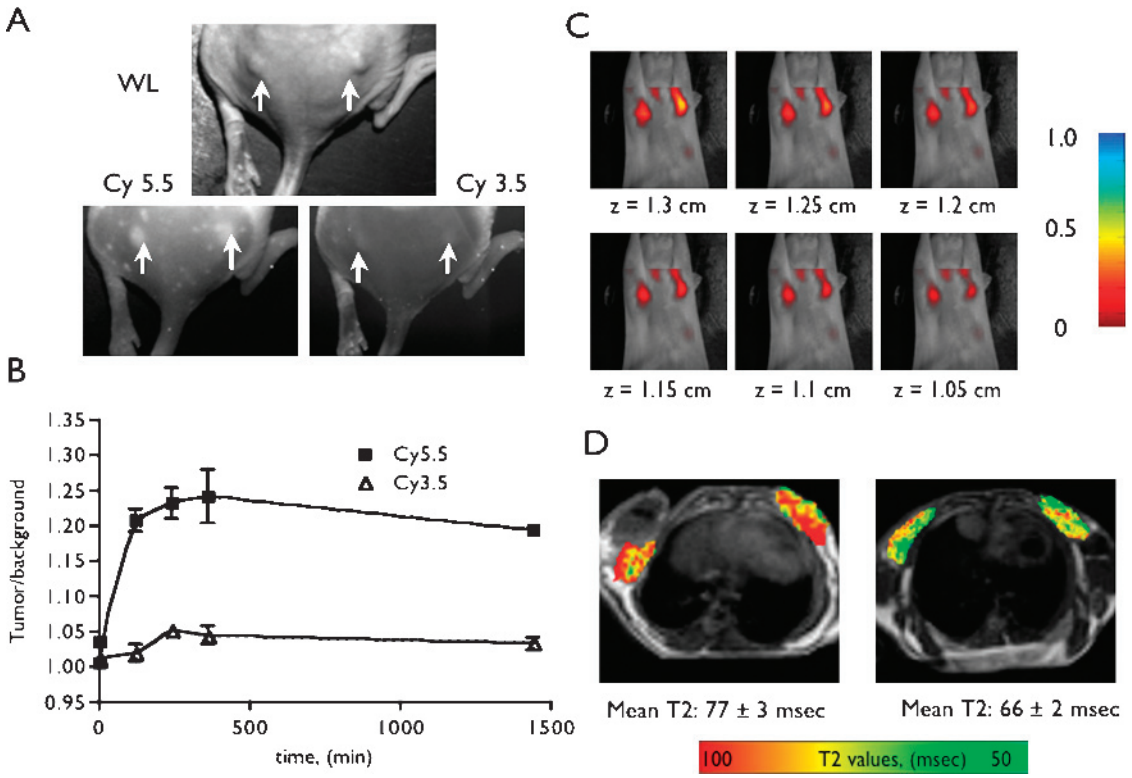

Figure 4. *Imaging the accumulation of the cRGD-CLIO(Cy5.5) nanoparticle by fluorescence and magnetic resonance. (A) White light and fluorescence reflectance images of implanted BT-20 tumors (two per animal). (B) Time dependence of tumor fluorescence determined by fluorescence reflectance, as shown in (A). (C) FMT images at indicated depths. Relative nanoparticle concentration in each plane. (D) MR imaging of nanoparticle accumulation in the tumor. Tumors are presented as colorized T2 maps superimposed over a T2-weighted MR image (TR = 2000; TE = 50) at 24 hours postinjection. Values are average tumor T2 values ± 1 SD.*

system consisted of 46 fibers spread over a 20 × 20 matrix in a slab geometry imaging chamber. For each fiber, four different sets of data were acquired (intrinsic fluorescence, extrinsic fluorescence, intrinsic noise, and fluorescence noise) through an ultralow-noise cooled charge-coupled device camera (Model 7471; Roper Scientific, Trenton, NJ). Images were acquired using a scattering medium consisting of 1% intralipid and 0.5% ink. Image acquisition time per animal was 3 to 5 minutes, and reconstruction time was approximately 10 minutes.

MR images were acquired on a 4.7-T Bruker imaging system (Pharmascan, Karlsruhe, Germany). T2-weighted sequences were obtained before and 24 hours after injection of cRGD-CLIO(Cy5.5) (3 mg/kg Fe). T2-weighted sequences were acquired with the following parameters: TR = 2000 milliseconds; TE = 6.5 to 104 milliseconds (16 different values); flip angle = 90°; matrix size = 128 × 64; average number = 4; field of view = 4.24 × 2.12 cm; slice thickness = 0.8 mm.

To visualize cRGD-CLIO(Cy5.5) tissue distribution (Figure 5), tissues were excised, snap-frozen, and cut into 10-μm sections. Air-dried slides were fixed in acetone at 4°C for 5 minutes. Fluorescence microscopy was performed on an Axiovert 100 TV system.

Avidin–biotin–based immunohistochemistry was used to identify endothelial cells (CD31), macrophages (CD11b), and $\alpha_V\beta_3$ integrins. Sections were stained with primary antibodies (anti-CD31 antibody from Santa Cruz Biotechnology; anti-CD11b from Serotec, Raleigh, NC; and anti-$\alpha_V\beta_3$ from Abcam, Inc.) and revealed with a biotinylated secondary antibody (Abcam, Inc.). Enzyme activity was developed for 8 minutes using Vectastain Elite ABC kit (Vector Laboratories, Burlingame, CA). Control sections were processed identically (omitting incubation with the primary antibody) and showed no staining.

For intravital microscopy (Figure 6), 10 nmol of the fluorochrome of cRGD-CLIO(Cy5.5) or cRGD was injected into nude mice through the tail vein. After median laparotomy, a section of sigmoid colon was exposed and imaged using a multichannel Radiance 2100 system (Bio-Rad, Richmond, CA) equipped with four lasers (×4 dry Nikon objective). Vessel fluorescence was recorded over time by operator-defined regions of blood vessel intensity, which were distinguishable from interstitial fluorescence by clearly defined anatomic margins. Blood half-life was then determined by fitting the data to a single exponential equation using GraphPad Prism (GraphPad Software, San Diego, CA).

Results

The components and functions of the cRGD-CLIO(Cy5.5) nanoparticle are shown schematically in Figure 1*A*. Figure 1*B* shows the syntheses and terminology for the peptides and nanoparticles used. For *in vitro* experiments (Figure 2*B*),

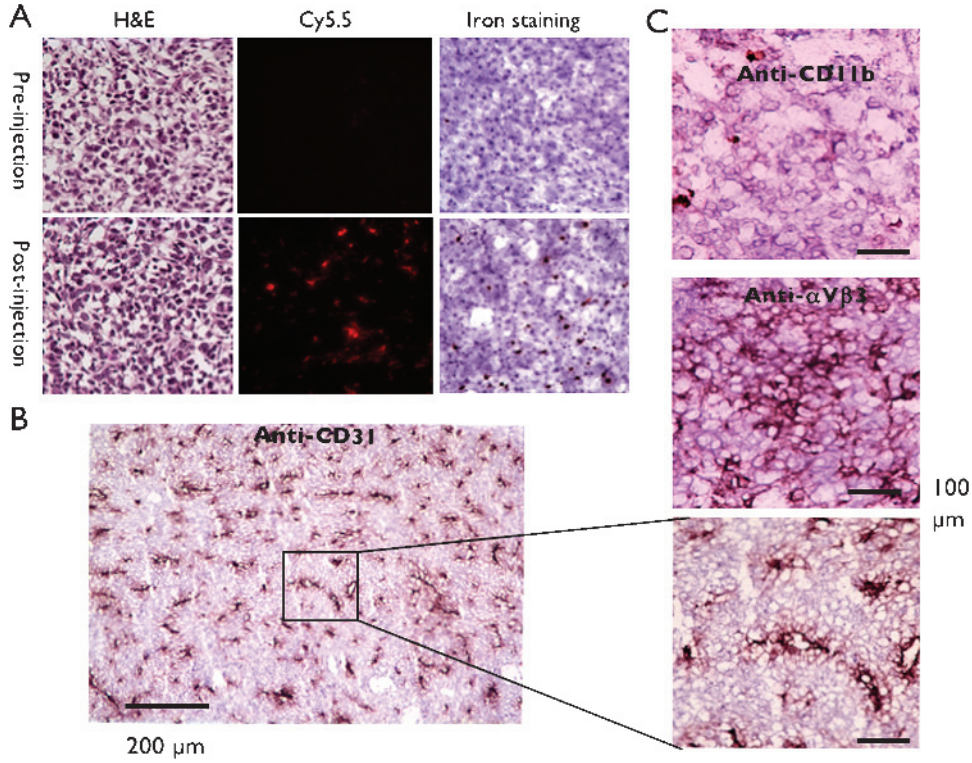

Figure 5. *Nanoparticle uptake by tumor cells of the BT-20 tumor. (A) The distribution of cRGD-CLIO(Cy5.5) within the tumor by iron stain or Cy5.5 fluorescence. After nanoparticle injection, iron and fluorescence are broadly distributed throughout the tumor. (B) Distribution of CD31 (endothelial cells) at low magnification. The tumor is highly vascularized. (C) Distribution of CD31 (endothelial cells), CD11b (macrophages), and $\alpha_V\beta_3$ by immunohistochemistry. There are a few macrophages in the tumor (CD11b). However, $\alpha_V\beta_3$ expressed in tumor cells is broadly distributed throughout the tumor, such as iron or Cy5.5 fluorescence from the nanoparticle.*

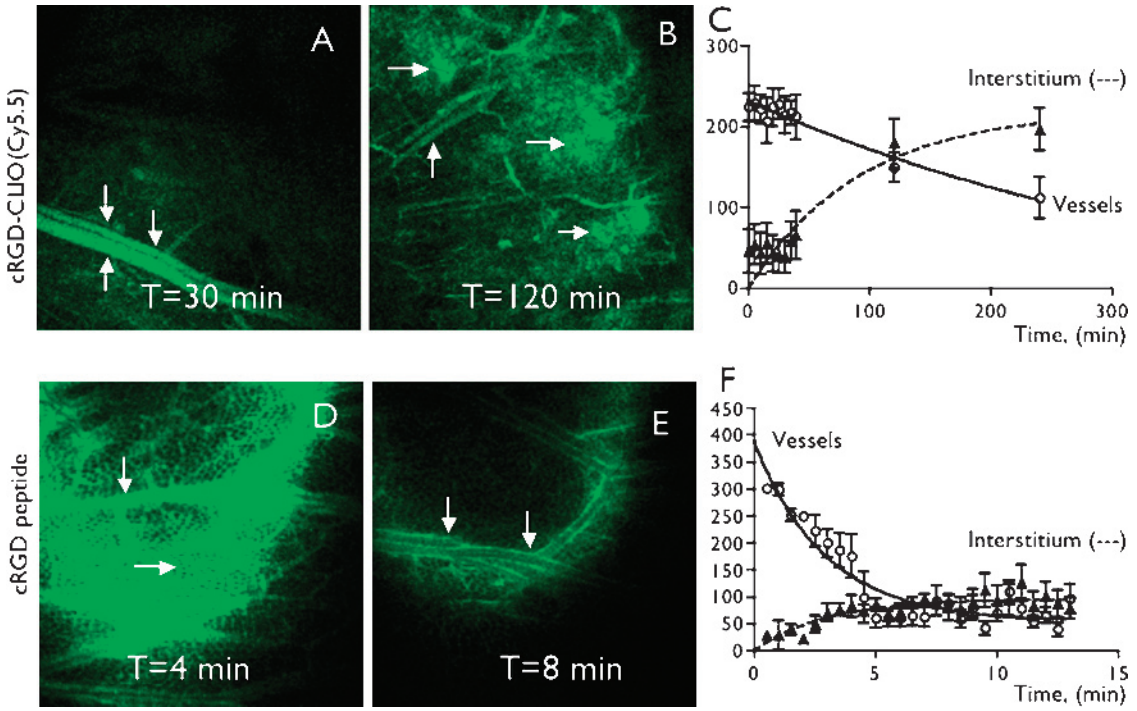

Figure 6. *Intravital microscopy of the exposed sigmoid colon after injection of the cRGD-CLIO(Cy5.5) nanoparticle or the cRGD. (A) Vessel and interstitial fluorescence 30 minutes after injection of cRGD-CLIO(Cy5.5). Nanoparticles are confined to the vasculature (vertical arrows). (B) Vessel and interstitial fluorescence at 120 minutes after nanoparticle injection. Nanoparticles are present in both the interstitium (horizontal arrows) and the vasculature (vertical arrows). (C) Time dependence of vessel fluorescence and interstitial fluorescence after injection of cRGD-CLIO(CY5.5). Images from (A) and (B) plus additional time points were used. (D) Vessel and interstitial fluorescence 4 minutes after injection of the cRGD. The peptide is already present in both the interstitium (horizontal arrow) and the vasculature (vertical arrow). (E) Vessel and interstitial fluorescence at 8 minutes after peptide injection. (F) Time dependence of vessel fluorescence and interstitial fluorescence after injection of the cRGD. Images from (D) and (E) plus additional time points were used.*

a control nanoparticle with reduced affinity for integrin was created by linearization of the cRGD with DTT. The Cy5.5 (or Cy3.5) fluorochrome and the superparamagnetic iron oxide core allow imaging of the nanoparticle *in vivo* by either fluorescence-based imaging or MRI. The cRGD can be linearized by treatment with DTT after conjugation to the nanoparticle, providing two nanoparticles that are matched in size, charge, and linking group, but differing in the conformation of the binding ligand. The RGD sequence is found in the loops of proteins [32], and cRGDs have roughly 10 to 100 higher affinity for their receptors than corresponding linear forms [33–35]. Decreased affinity on linearization provides a convenient method of demonstrating integrin-mediated uptake, especially because the monovalent cRGD does not block the uptake of the multivalent cRGD-CLIO nanoparticle due to multivalent interactions (Montet and Josephson, unpublished observations). However, the lRGD retained some affinity for cells; thus, for *in vitro* specificity studies (Figure 3), a scrambled linear peptide was employed (scrRGD). The physical properties of the nanoparticles are provided in Figure 1*C*, along with the biologic properties of blood half-life. cRGD-CLIO(Cy5.5) has a blood half-life of 180 minutes, compared to the blood half-life of the parent CLIO nanoparticle, which was 640 minutes using an radiolabeled nanoparticle [36] and 508 minutes using the intravital vessel fluorescence method employed here.

We examined BT-20 cells for their expression of the $\alpha_V\beta_3$ integrin and their ability to bind cRGD (the cyclic peptide used in nanoparticle synthesis), using a dual-wavelength fluorescence-activated cell sorter (FACS), as shown in Figure 2*A*. $\alpha_V\beta_3$ Integrins are expressed in endothelial cells [37,38], but they are also present in a variety of tumor cells [39,40]. BT-20 cells bound both anti-$\alpha_V\beta_3$ and the cRGD to high levels, but not anti-CD31—an antibody to a marker expressed in endothelial cells. The expression of $\alpha_V\beta_3$ on BT-20 cells was also evident from the binding of cRGD-CLIO(Cy5.5) with an EC_{50} of 0.0113 μM, as shown in Figure 2*B*. When the nanoparticle was treated with DTT to linearize the peptide, the EC_{50} dropped by about 40-fold, as was expected based on the higher affinity of cRGD (see above). As shown in Figure 2*C*, the 9L tumor expressed about 20% of the cRGD binding obtained with BT-20 cells, as determined by analysis of the data for maximum binding.

We then determined the molecular specificity of cRGD-CLIO(Cy5.5) for $\alpha_V\beta_3$ *in vivo* by injecting 5 mg/kg Fe of a mixture of the integrin-targeted nanoparticle cRGD-CLIO(Cy5.5) and control scrRGD-CLIO(Cy3.5) in animals bearing either the BT-20 or the 9L tumors. (The same amount of fluorescence from each fluorochrome was injected.) Figure 3, *A* and *B*, shows tissue fluorescence in the Cy5.5 and Cy3.5 channels of injected and uninjected animals, whereas Figure 3*C* shows the ratio of the two amounts of fluorescence (autofluorescence subtracted) in these channels. The BT-20 tumor had a uniquely high Cy5.5/Cy3.5 fluorescence ratio of 6.5, whereas the liver and spleen, which accumulated both nanoparticles to high

concentrations, had fluorescence ratios around 1, corresponding to nonspecific uptake of both nanoparticles. The Cy5.5/Cy3.5 fluorescence ratio of BT-20 tumors differed from all organs and from the 9L tumor at a level of $P < .001$. The 9L tumor, with about 20% of the integrin of the BT-20 tumor, had a Cy5.5/Cy3.5 fluorescence ratio of 1.8, which was higher than the ratio of fluorescence of the organs, but this value did not reach the significant level ($P > .50$).

We then imaged $\alpha_V\beta_3$ integrin expression in the BT-20 tumor by FRI, FMT, and MRI after injection of the nanoparticle mixture used in Figure 3. As shown in Figure 4*A*, FRI showed a higher fluorescence in the Cy5.5 channel than in the Cy3.5 channel, as was expected from fluorescence reflectance data on dissected tumor tissues (Figure 3*C*). The time course of BT-20 tumor fluorescence by FRI for the Cy5.5 and Cy3.5 channels is shown in Figure 4*B*. Because the blood half-life of the agent is 180 minutes (see below and Figure 1*C*), tumor fluorescence from early time points reflects the nanoparticle in the vasculature (Figure 6). By 1500 minutes postinjection, the agent was no longer in the vasculature, and the tumor fluorescence was due to nanoparticle accumulation in tumor cells (see Figure 5*A*). We then injected 3 mg/kg Fe of cRGD-CLIO(Cy5.5) to obtain FMT images at various depths (Figure 4*C*), showing the concentration of nanoparticle in each plane. A T2-weighted MR image of the BT-20 tumors at 3 mg/kg Fe of the BT-20 tumor is shown in Figure 4*D*. The mean tumor T2 dropped from 77 to 66 milliseconds with the uptake of the nanoparticle.

The distribution of the cRGD-CLIO(Cy5.5) nanoparticle in the BT-20 tumor was examined with iron staining and fluorescence microscopy, as shown in Figure 5*A*. Tumors from uninjected animals showed no visible Cy5.5 fluorescence or iron accumulation, whereas tumors from injected animals showed both iron and Cy5.5 fluorescence throughout the tumor. We next characterized the vascularity of the tumor using CD31 (endothelial cell marker) at low magnification, as shown in Figure 5*B*. The BT-20 tumor is highly vascularized, with numerous small capillaries separated by distances of <100 μm in-between. We then characterized the BT-20 tumor for the presence of CD11b (a macrophage marker) and CD31 (an endothelial cell maker), as well as for $\alpha_V\beta_3$ at higher magnifications, as shown in Figure 5*C*. As expected based on the presence of $\alpha_V\beta_3$ integrins on BT-20 cells determined by FACS (Figure 2*A*), the $\alpha_V\beta_3$ integrin was widely distributed through the tumor. The diffuse pattern of iron and Cy5.5 fluorescence after injection of the cRGD-CLIO(Cy5.5) nanoparticle correlated with $\alpha_V\beta_3$ expression on tumor cells and is further discussed below.

Intravital microscopy of the exposed sigmoid colon was employed to visualize the disposition of the cRGD-CLIO(Cy5.5) nanoparticle and to compare the disposition of the nanoparticle and cRGD, as shown in Figure 6. At 30 minutes postinjection (Figure 6*A*), the nanoparticle was still in the vasculature (vertical arrows); by 120 minutes (Figure 6*B*), it was present in the vasculature (vertical arrows) and interstitium (horizontal arrows). The time course of vessel and interstitial fluorescence is shown in Figure 6*C*. Vessel fluorescence was analyzed according to a single exponential decay model and yielded a half-life of 180 minutes. Interstitial fluorescence increased steadily up to 220 minutes—the longest time point obtained. In contrast, the cRGD was present in both the vasculature and the interstitium at 4 minutes postinjection (Figure 6*D*). By 8 minutes postinjection (Figure 6*E*), the peptide had largely cleared from the vessel and interstitium, and had a blood half-life of 13 minutes. cRGD-CLIO(Cy5.5) had a moderately long blood half-life of 180 minutes and escaped from the vasculature. As control, the blood half-life of amino-CLIO was determined to be 508 minutes, which compared well with a half-life of 640 minutes determined earlier with a radiolabeled amino-CLIO [36].

Discussion

The molecular specificity of cRGD-CLIO(Cy5.5) nanoparticle *in vitro* was indicated by the reduced affinity of the nanoparticle with the IRGD (Figure 2), and *in vivo* by the high ratio of cRGD-CLIO(Cy5.5)/scrRGD-CLIO(Cy3.5) accumulation in the BT-20 tumor (Figure 3*C*). The dual nanoparticle/fluorescence ratio method is useful for determining molecular specificity *in vivo* because targeting is defined as the "extra" accumulation of targeted *versus* nontargeted nanoparticles. Nontargeted magnetic nanoparticles accumulate not only in the major organs of the reticuloendothelial system (liver and spleen), but also in tumors [41–43] and many tissues when inflamed [44–47]. Because of strong multivalent affinity enhancement, the binding of the cRGD-CLIO nanoparticle to cells cannot be blocked by monovalent RGD (Montet and Josephson, in preparation).

Our results indicate that the predominant cell internalizing the cRGD-CLIO(Cy5.5) nanoparticle in the BT-20 tumor is the tumor cell. First, the $\alpha_V\beta$ integrin (not CD31) was present on cultured BT-20 cells as determined by FACS (Figure 2), and tumor cells internalized cRGD-CLIO(Cy5.5) (see Figure 2). Second, immunohistochemistry indicated that the $\alpha_V\beta$ integrin was broadly distributed throughout the tumor (Figure 6*C*), whereas endothelial cells, visualized by CD31, were present as discrete structures within the tumor (i.e., as capillaries) (Figure 6*B*). The distribution of the cRGD-CLIO(Cy5.5) nanoparticle, examined by either iron stain or fluorescence microscopy, was broad and dissimilar from the distribution of CD31/endothelial cells. These results do not imply that the cRGD-CLIO(Cy5.5) is not internalized by endothelial cells, but that the major cell accumulating the cRGD-CLIO(Cy5.5) in the BT-20 tumor is the tumor cell.

The cRGD-CLIO(Cy5.5) nanoparticle was readily detectable by fluorescence-based imaging (FRI and FMT) and MR-based imaging at a dose (3 mg/kg Fe) compatible with human use. To avoid iron-related toxicity in humans, the dose of iron-based diagnostic agents is generally kept below 3 mg/kg Fe (54 μmol/kg Fe), or about 5% of the total body iron (70-kg male with 4000 mg of Fe) [48]. The limit on iron dose, together with limits on the amount of fluorochrome that can be attached to the nanoparticle, confines the dose of fluorochrome. The number of fluorochromes per nanoparticle is limited by intrafluorochrome-related quenching (Josephson

and Reynolds, unpublished observations), so that the fluorochrome/iron ratio is typically about one fluorochrome per 1000 Fe (eight per nanoparticle at 8000 Fe/nanoparticle, or 54 nmol/kg at 3 mg/kg Fe). Thus, for targeted magneto-optical nanoparticles to be considered for clinical use, they must be detectable by fluorescent and MRI modalities at iron doses below 3 mg/kg Fe.

Our results also suggest that nanoparticles could be targeted to molecular markers (other than integrins) that are expressed in tumor cells, if the nanoparticle and the tumor have characteristics similar to those employed here. We identified three factors associated with the ability of the cRGD-CLIO(Cy5.5) nanoparticle to target integrins expressed in tumor cells:

Tumor cell integrin expression: $\alpha_V\beta_3$ integrin was expressed in BT-20 tumor cells, and these cells internalized the nanoparticle with a low EC_{50} for nanoparticles *in vitro*. Using both dissected tissue fluorescence reflectance measurements (Figure 3*C*) and *in vivo* tumor fluorescence reflectance (Figure 4*B*), the accumulation of cRGD-CLIO(Cy5.5) by the BT-20 tumor exceeded that of the 9L tumor; this, in turn, correlated with the higher expression of $\alpha_V\beta_3$ by the BT-20 tumor (Figure 2*C*). Both tumors were used during the rapid growth phase (with a diameter of approximately 1 to 2 mm) and had a high density of capillaries.

Nanoparticle pharmacokinetics: The blood half-life of the cRGD-CLIO(Cy5.5) was 180 minutes (Figure 1*C*), which was sufficient to allow vascular escape (Figure 6*C*) and targeting of the nanoparticle to the $\alpha_V\beta_3$ expressed in tumor cells (Figures 2*C* and 4*D*). The nanoparticle was too large to undergo renal elimination characteristic of low-molecular-weight materials and was eventually cleared from the blood by macrophages of the liver and spleen. The accumulation of iron oxide–based nanoparticles (such as those employed here) by the liver and spleen was typically without toxic effects because such organs are involved in normal iron storage and degradation. After accumulation in the liver and spleen, iron oxide–based nanoparticles, such as those employed here, were degraded and the iron was incorporated into red blood cells [49].

Tumor vascularization: The BT-20 tumor had a dense capillary bed (Figure 5*B*), with distances of <100 μm between capillaries.

Our finding that the cRGD-CLIO(Cy5.5) nanoparticle can image integrins expressed in tumor cells suggests a variety of approaches that may be possible for a tumor-targeted RGD nanoparticle–based diagnostic agent:

Continued development of magneto-fluorescent nanoparticles targeted to the $\alpha V\beta 3$ integrin: Integrin-targeted magneto-fluorescent nanoparticles can provide precontrast MR images and intraoperative fluorescent images—a paradigm that might be useful for a more accurate margin delineation [50]. Continued development of a nanoparticle-based fluorescent or magnetic imaging agent could involve replacing disulfide-linked cRGD with a low-molecular-weight head-to-tail cRGD [51] or with an RGD peptidomimetic [52,53]. Head-to-tail cyclized RGD may have higher affinities for integrins than the disulfide-linked cRGD we employed due to greater conformational rigidity, optimization of amino acids adjacent to the RGD sequence, or resistance to formation of IRGDs, which have lower affinities for integrins.

Development of a magnetic nanoparticle targeted to the $\alpha_V\beta_3$ integrin: The fluorochrome, used to follow nanoparticle disposition *in vitro* or *in vivo*, might be removed and a peptide may be attached to a dextran-coated iron oxide core. Dextran-coated iron oxides are the basis of approved MR contrast agents and iron preparation used for the treatment of anemia, suggesting that RGD nanoparticles for clinical use could be based on a modification of the basic design shown in Figure 1*A*.

Development of a fluorescent nanoparticle targeted to the $\alpha_V\beta_3$ integrin: Non–iron-bearing fluorescent nanoparticles have been described with several different designs and have been used in animal imaging [54–56].

Development of a multifunctional (therapeutic and diagnostic) nanoparticle targeted to the $\alpha_V\beta_3$ integrin: Finally, the RGD-CLIO(Cy5.5) nanoparticle is highly active in the antiendothelial cell adhesion assay used to assess the potency of integrin-targeted antiangiogenic therapeutic agents (Montet and Josephson, submitted for publication). The ability to image the disposition of an RGD-therapeutic agent may assist in the prediction of its effectiveness in specific individuals.

References

[1] Ferrari M (2005). Cancer nanotechnology: opportunities and challenges. *Nat Rev Cancer* **5,** 161–171.

[2] NCI/NIH (2004). *Cancer Nanotechnology Plan, A Strategic Initiative to Transform Clinical Oncology and Basic Research through Directed Application of Nanotechnology.* (http://nano.cancer.gov/) Washington, DC, pp. 8–9.

[3] Moghimi SM, Hunter AC, and Murray JC (2005). Nanomedicine: current status and future prospects. *FASEB J* **19,** 311–330.

[4] Reynolds F, O'Loughlin T, Weissleder R, and Josephson L (2005). Method of determining nanoparticle core weight. *Anal Chem* **77,** 814–817.

[5] Zhao M, Kircher MF, Josephson L, and Weissleder R (2002). Differential conjugation of tat peptide to superparamagnetic nanoparticles and its effect on cellular uptake. *Bioconjug Chem* **13,** 840–844.

[6] Schellenberger EA, Sosnovik D, Weissleder R, and Josephson L (2004). Magneto/optical annexin V, a multimodal protein. *Bioconjug Chem* **15,** 1062–1067.

[7] Kitov PI and Bundle DR (2003). On the nature of the multivalency effect: a thermodynamic model. *J Am Chem Soc* **125,** 16271–16284.

[8] Wright D and Usher L (2001). Multivalent binding in the design of bioactive compounds. *Curr Org Chem* **5,** 1107–1131.

[9] Mammen M, Chio S-K, and Whitesides GM (1998). Polyvalent interactions in biological systems: implications for design and use of multivalent ligands and inhibitors. *Angew Chem Int Ed Engl* **37,** 2755–2794.

[10] Munson PJ and Rodbard D (1979). Computer modeling of several ligands binding to multiple receptors. *Endocrinology* **105,** 1377–1381.

[11] Jain RK (1997). Delivery of molecular and cellular medicine to solid tumors. *Adv Drug Deliv Rev* **26,** 71–90.

[12] Jain RK (1990). Tumor physiology and antibody delivery. *Front Radiat Ther Oncol* **24,** 32–46 (discussion, 64–68).

[13] Winter PM, Morawski AM, Caruthers SD, Fuhrhop RW, Zhang H, Williams TA, Allen JS, Lacy EK, Robertson JD, Lanza GM, et al. (2003). Molecular imaging of angiogenesis in early-stage atherosclerosis with alpha(v)beta3-integrin–targeted nanoparticles. *Circulation* **108,** 2270–2274.

[14] Hood JD, Bednarski M, Frausto R, Guccione S, Reisfeld RA, Xiang R,

et al. (2002). Tumor regression by targeted gene delivery to the neovasculature. *Science* **296,** 2404–2407.
[15] Hallahan D, Geng L, Qu S, Scarfone C, Giorgio T, Donnelly E, et al. (2003). Integrin-mediated targeting of drug delivery to irradiated tumor blood vessels. *Cancer Cell* **3,** 63–74.
[16] Anderson SA, Rader RK, Westlin WF, Null C, Jackson D, Lanza GM, et al. (2000). Magnetic resonance contrast enhancement of neovasculature with alpha(v)beta(3)–targeted nanoparticles. *Magn Reson Med* **44,** 433–439.
[17] Arap W, Pasqualini R, and Ruoslahti E (1998). Cancer treatment by targeted drug delivery to tumor vasculature in a mouse model. *Science* **279,** 377–380.
[18] Yu X, Song SK, Chen J, Scott MJ, Fuhrhop RJ, Hall CS, et al. (2000). High-resolution MRI characterization of human thrombus using a novel fibrin-targeted paramagnetic nanoparticle contrast agent. *Magn Reson Med* **44,** 867–872.
[19] Schmieder AH, Winter PM, Caruthers SD, Harris TD, Williams TA, Allen JS, et al. (2005). Molecular MR imaging of melanoma angiogenesis with alpha(nu)beta(3)–targeted paramagnetic nanoparticles. *Magn Reson Med* **53,** 621–627.
[20] Kelly KA, Allport JR, Tsourkas A, Shinde-Patil VR, Josephson L, and Weissleder R (2005). Detection of vascular adhesion molecule-1 expression using a novel multimodal nanoparticle. *Circ Res* **96,** 327–336.
[21] Hall CS, Marsh JN, Scott MJ, Gaffney PJ, Wickline SA, and Lanza GM (2000). Time evolution of enhanced ultrasonic reflection using a fibrin-targeted nanoparticulate contrast agent. *J Acoust Soc Am* **108,** 3049–3057.
[22] Josephson L, Perez JM, and Weissleder R (2001). Magnetic nanosensors for the detection of oligonucleotide sequences. *Angew Chem Int Ed Engl* **40,** 3204–3206.
[23] Josephson L, Tung CH, Moore A, and Weissleder R (1999). High-efficiency intracellular magnetic labeling with novel superparamagnetic–Tat peptide conjugates. *Bioconjug Chem* **10,** 186–191.
[24] Koch AM, Reynolds F, Kircher MF, Merkle HP, Weissleder R, and Josephson L (2003). Uptake and metabolism of a dual fluorochrome Tat-nanoparticle in HeLa cells. *Bioconjug Chem* **14,** 1115–1121.
[25] Tsourkas A, Hofstetter O, Hofstetter H, Weissleder R, and Josephson L (2004). Magnetic relaxation switch immunosensors detect enantiomeric impurities. *Angew Chem Int Ed Engl* **43,** 2395–2399.
[26] Kelly KA, Reynolds F, Weissleder R, and Josephson L (2004). Fluorescein isothiocyanate–hapten immunoassay for determination of peptide–cell interactions. *Anal Biochem* **330,** 181–185.
[27] Mahmood U, Tung CH, Bogdanov A Jr, and Weissleder R (1999). Near-infrared optical imaging of protease activity for tumor detection. *Radiology* **213,** 866–870.
[28] Mahmood U, Tung CH, Tang Y, and Weissleder R (2002). Feasibility of *in vivo* multichannel optical imaging of gene expression: experimental study in mice. *Radiology* **224,** 446–451.
[29] Graves EE, Ripoll J, Weissleder R, and Ntziachristos V (2003). A submillimeter resolution fluorescence molecular imaging system for small animal imaging. *Med Phys* **30,** 901–911.
[30] Ntziachristos V and Weissleder R (2001). Experimental three-dimensional fluorescence reconstruction of diffuse media by use of a normalized Born approximation. *Opt Lett* **26,** 893–895.
[31] Ntziachristos V, Schellenberger EA, Ripoll J, Yessayan D, Graves E, Bogdanov A Jr, et al. (2004). Visualization of antitumor treatment by means of fluorescence molecular tomography with an annexin V–Cy5.5 conjugate. *Proc Natl Acad Sci USA* **101,** 12294–12299.
[32] Kuhn K and Eble J (1994). The structural bases of integrin–ligand interactions. *Trends Cell Biol* **4,** 256–261.
[33] Gurrath M, Muller G, Kessler H, Aumailley M, and Timpl R (1992). Conformation/activity studies of rationally designed potent anti-adhesive RGD peptides. *Eur J Biochem* **210,** 911–921.
[34] Aumailley M, Gurrath M, Muller G, Calvete J, Timpl R, and Kessler H (1991). Arg–Gly–Asp constrained within cyclic pentapeptides. Strong and selective inhibitors of cell adhesion to vitronectin and laminin fragment P1. *FEBS Lett* **291,** 50–54.
[35] Haubner R, Gratias R, Diefenbach B, Goodman SL, Jonczyk A, and Kessler H (1996). Structural and functional aspects of RGD-containing cyclic pentapeptides as highly potent and selective integrin alpha$_V$beta$_3$ antagonists. *J Am Chem Soc* **118,** 7461–7472.
[36] Wunderbaldinger P, Josephson L, and Weissleder R (2002). Tat peptide directs enhanced clearance and hepatic permeability of magnetic nanoparticles. *Bioconjug Chem* **13,** 264–268.
[37] Brooks PC (1996). Role of integrins in angiogenesis. *Eur J Cancer* **32A,** 2423–2429.
[38] Stromblad S and Cheresh DA (1996). Cell adhesion and angiogenesis. *Trends Cell Biol* **6,** 462–468.
[39] Pasqualini R, Koivunen E, and Ruoslahti E (1997). Alpha v integrins as receptors for tumor targeting by circulating ligands. *Nat Biotechnol* **15,** 542–546.
[40] Cheresh DA, Pytela R, Pierschbacher MD, Klier FG, Ruoslahti E, and Reisfeld RA (1987). An Arg–Gly–Asp–directed receptor on the surface of human melanoma cells exists in an divalent cation–dependent functional complex with the disialoganglioside GD2. *J Cell Biol* **105,** 1163–1173.
[41] Jonkmanns C, Saleh A, Rees M, and Moedder U (2002). Ultrasmall superparamagnetic iron oxide MRI of head and neck cancer: enhancement of primary tumor and influence on T staging. *Radiology* **225,** 281 (Supplement).
[42] Enochs WS, Harsh G, Hochberg F, and Weissleder R (1999). Improved delineation of human brain tumors on MR images using a long-circulating, superparamagnetic iron oxide agent. *J Magn Reson Imaging* **9,** 228–232.
[43] Varallyay P, Nesbit G, Muldoon LL, Nixon RR, Delashaw J, Cohen JI, et al. (2002). Comparison of two superparamagnetic viral-sized iron oxide particles ferumoxides and ferumoxtran-10 with a gadolinium chelate in imaging intracranial tumors. *AJNR Am J Neuroradiol* **23,** 510–519.
[44] Schmitz SA, Taupitz M, Wagner S, Wolf KJ, Beyersdorff D, and Hamm B (2001). Magnetic resonance imaging of atherosclerotic plaques using superparamagnetic iron oxide particles. *J Magn Reson Imaging* **14,** 355–361.
[45] Trivedi R, U-King-Im J, and Gillard J (2003). Accumulation of ultrasmall superparamagnetic particles of iron oxide in human atherosclerotic plaque. *Circulation* **108,** e140 (author reply, e140).
[46] Saleh A, Schroeter M, Jonkmanns C, Hartung HP, Modder U, and Jander S (2004). *In vivo* MRI of brain inflammation in human ischaemic stroke. *Brain* **127,** 1670–1677.
[47] Lutz AM, Seemayer C, Corot C, Gay RE, Goepfert K, Michel BA, et al. (2004). Detection of synovial macrophages in an experimental rabbit model of antigen-induced arthritis: ultrasmall superparamagnetic iron oxide–enhanced MR imaging. *Radiology* **233,** 149–157.
[48] Politou P and Papanikolaou G (2004). Hepcidin: a key regulator involved in the pathogenesis of anemia of chronic disease. *Haema* **7,** 165–174.
[49] Weissleder R, Stark DD, Engelstad BL, Bacon BR, Compton CC, White DL, et al. (1989). Superparamagnetic iron oxide: pharmacokinetics and toxicity. *AJR Am J Roentgenol* **152,** 167–173.
[50] Kircher MF, Mahmood U, King RS, Weissleder R, and Josephson L (2003). A multimodal nanoparticle for preoperative magnetic resonance imaging and intraoperative optical brain tumor delineation. *Cancer Res* **63,** 8122–8125.
[51] Dechantsreiter MA, Planker E, Matha B, Lohof E, Holzemann G, Jonczyk A, et al. (1999). *N*-methylated cyclic RGD peptides as highly active and selective alpha(V)beta(3) integrin antagonists. *J Med Chem* **42,** 3033–3040.
[52] Andronati SA, Karaseva TL, and Krysko AA (2004). Peptidomimetics—antagonists of the fibrinogen receptors: molecular design, structures, properties and therapeutic applications. *Curr Med Chem* **11,** 1183–1211.
[53] Haubner R, Finsinger D, and Kessler H (1997). Stereoisomeric peptide libraries and peptidomimetics for designing selective inhibitors of the alpha$_v$beta$_3$ integrin for a new cancer therapy. *Angew Chem Int Ed Engl* **36,** 1374–1389.
[54] Gao X, Cui Y, Levenson RM, Chung LW, and Nie S (2004). *In vivo* cancer targeting and imaging with semiconductor quantum dots. *Nat Biotechnol* **22,** 969–976.
[55] Santra S, Liesenfeld B, Dutta D, Chatel D, Batich CD, Tan W, et al. (2005). Folate conjugated fluorescent silica nanoparticles for labeling neoplastic cells. *J Nanosci Nanotechnol* **5,** 899–904.
[56] Ow H, Larson DR, Srivastava M, Baird BA, Webb WW, and Wiesner U (2005). Bright and stable core–shell fluorescent silica nanoparticles. *Nano Lett* **5,** 113–117.